Dynamic viability of the 2016 Mw 7.8 Kaikōura earthquake cascade on weak crustal faults

Thomas Ulrich*[1], Alice-Agnes Gabriel[1], Jean-Paul Ampuero[2] and Wenbin Xu[3]

* ulrich@geophysik.uni-muenchen.de

1 Department of Earth and Environmental Sciences, Ludwig-Maximilians-Universität München, Germany

2 Seismological Laboratory, California Institute of Technology, USA

Now at: Université Côte d'Azur, IRD, CNRS, Observatoire de la Côte d'Azur, Géoazur, France

3 Department of Land Surveying and Geo-Informatics, Hong Kong Polytechnic University, Hong Kong, China

Abstract

The Mw 7.8 Kaikōura earthquake struck New Zealand's South Island on November 14, 2016. This event, considered the most complex rupture observed to date, caused surface rupture of at least 21 segments of the Marlborough fault system, some of them previously unknown. Puzzling features inferred from high-quality observations include a large gap separating surface rupture traces, the possibility of significant slip on the subduction interface, and slow apparent rupture speed. Here we develop a dynamic rupture model to unravel the event's riddles in a physics-based manner. Our model reproduces key characteristics of the event and provides insights on the mechanical viability of competing hypotheses proposed to explain them. We show that the observed rupture cascade, involving strike and thrust faulting, is dynamically consistent with regional stress estimates and a crustal fault network geometry inferred from seismic and geodetic data. The rupture propagation requires a linking low-dipping shallow thrust fault, but not slip on an underlying megathrust. The complex fault system operates at low apparent friction thanks to the combined effects of overpressurized fluids, low dynamic friction and stress concentrations induced by deep fault creep.

Observational studies of the Kaikōura earthquake based on geological, geodetic, tsunami and seismic data reveal puzzling features. An apparent gap of 15-20 km between known fault structures (Hamling et al., 2017) may suggest a rupture jump over an unexpectedly large distance or the presence of deep fault segments connecting surface rupturing faults. Rupture duration is long, more than twice the average duration of past earthquakes of same magnitude (Duputel and Rivera, 2017). Finite-fault source inversion models inferred from strong motion and other data (Bradley et al. (2017), Holden et al. (2017) and Wang et al. (2018)) present unconventional kinematic features, such as unusually large delays between segments (Bradley et al., 2017) or strong scatter in the distribution of rupture time (Wang et al., 2018). The rupture may include simultaneous slip on the Hikurangi subduction interface (Wang et al., 2018) and several segments slipping more than once (Holden et al., 2017).

Competing views of the Kaikōura earthquake have emerged from previous studies. Teleseismic back-projection studies (Hollingsworth et al. (2017), Xu et al. (2018), Zhang et al. (2017)) agree on general earthquake characteristics (e.g. an overall SW-NE propagation direction) but not on the space-time evolution of the rupture. Whereas far-field teleseismic and some tsunami data inferences require thrust faulting on a low dipping fault, interpreted as the subduction interface beneath the Upper Kowhai and Jordan Thrust faults (Bai et al., 2017, Hollingsworth et al., 2017, Duputel and Rivera, 2017, Wang et al., 2018), analysis of strong motion, aftershocks, geodetic and coastal deformation observations find little or no contribution of the subduction interface (Holden et al., 2017, Clark et al., 2017, Ceska et al., 2017, Xu et al., 2018). The geometry of the Hikurangi megathrust is not well constrained in its Southern end (Williams et al., 2013): dipping angles assumed in previous studies range from 12 to 25 degrees (Hamling et al., 2017; Wang et al., 2018). Large-scale ground-deformations have then been explained by either slip on the subduction interface (e.g. Hamling et al., 2017, Wang et al., 2018) or by refined crustal models featuring listric fault geometries (Xu et al., 2018) or shallow thrust faults (Clark et al., 2017).

Incorporating the requirement that the rupture should be dynamically viable can help constrain the unexpected features and competing views of this event. Analyses of static Coulomb failure stress changes during rupture provides some mechanical insight on the rupture sequence (Hamling et al. (2017), Xu et al. (2018)), but do not account for dynamic stress changes, which are an important factor in multi-fault ruptures (e.g., Bai and Ampuero, 2017). Dynamic rupture simulations provide physically self-consistent earthquake source descriptions, and have been used to study fundamental aspects of earthquake physics (e.g. Gabriel et al., 2012, Shi and Day, 2013), to assess earthquake hazard (e.g., Aochi and Ulrich, 2015) and to understand previous earthquakes (e.g. Olsen et al. (1997), Ma et al. (2008)). The dynamic rupture modelling presented here provides physical arguments to discriminate between competing models of the fault system geometry and faulting mechanisms.

Much like the San Andreas fault, the Marlborough fault system is apparently weak, according to its large angle relative to the maximum horizontal compressive stress (Townend et al., 2012). The apparent weakness of faults, a major conundrum in tectonics (e.g. Brune et al. (1969), Copley (2018)), can be reconciled with the high static strength implied by Byerlee’s law (Byerlee, 1978) by considering dynamic weakening, which allows faults to operate at low average shear stress. However, low background stresses are generally unfavourable for rupture cascading. For instance, rupture jumps across fault stepovers are hindered by low initial stresses (Bai and Ampuero, 2017). This is one reason why finding a viable dynamic rupture model is non-trivial.

Our dynamic model of the Kaikōura earthquake is tightly determined by integrating knowledge and data spanning a broad range of scales. It combines an unprecedented degree of realism, including a modern laboratory-based friction law, off-fault inelasticity, seismological estimates of regional stress, a realistic fault network geometry model, a 3D subsurface velocity model and high-resolution topography and bathymetry. High resolution 3D modeling is enabled by a software that couples seismic wave propagation with frictional fault failure and off-fault inelasticity, optimized for high-performance computing. The resulting dynamic model of the Kaikōura earthquake sheds light on the physical mechanisms of cascading ruptures in complex fault systems.

1. Model

1.1 Fault geometry

We construct a model of the non-planar, intersecting network of crustal faults (fig. 1) by combining constraints from previous observational studies and from dynamic rupture modeling experiments. Fault geometries and orientations have been constrained by geological and geodetic data (e.g. Litchfield et al., 2012, Xu et al., 2018). Our starting point is a smoothed version of the fault network geometry “model III” inferred from field and remote sensing data by Xu et al. (2018). It comprises three strike-slip faults: Humps and Stone Jug fault and a long segment with listric geometry (flattening at depth) resembling jointly Hope-Upper Kowhai-Jordan Thrust, Kekerengu and Needles faults; and four thrust faults: Conwell-Charwell, Hundalee, Point Kean and Papatea faults. The model does not include the subduction interface but is sufficient to explain the observed static ground deformations in the near and far-field.

Based on dynamic rupture experiments we remove the Southern part of Hope and the complete Upper Kowhai fault. Both faults are well oriented and experience considerable slip upon their inclusion in contradiction with observations. Additionally, a direct rupture path from the Hope fault to the Jordan Thrust via the Upper Kowhai fault needs to be prevented (fig. S1) to match the timing of the dominant peak in moment release which is clearly associated with the rupture of the Kekerengu fault in both kinematic source inversions (e.g. Holden et al., 2017) and our model. Instead, we postulate that the previously unknown Point Kean fault (Clark et al., 2017) acted as a crucial link between the Hundalee Fault and the Northern faults. The Northern part of the Hope fault which experienced surface rupture is dynamically necessary for rupture to breach the gap between the Conway-Charwell and Stone Jug faults.

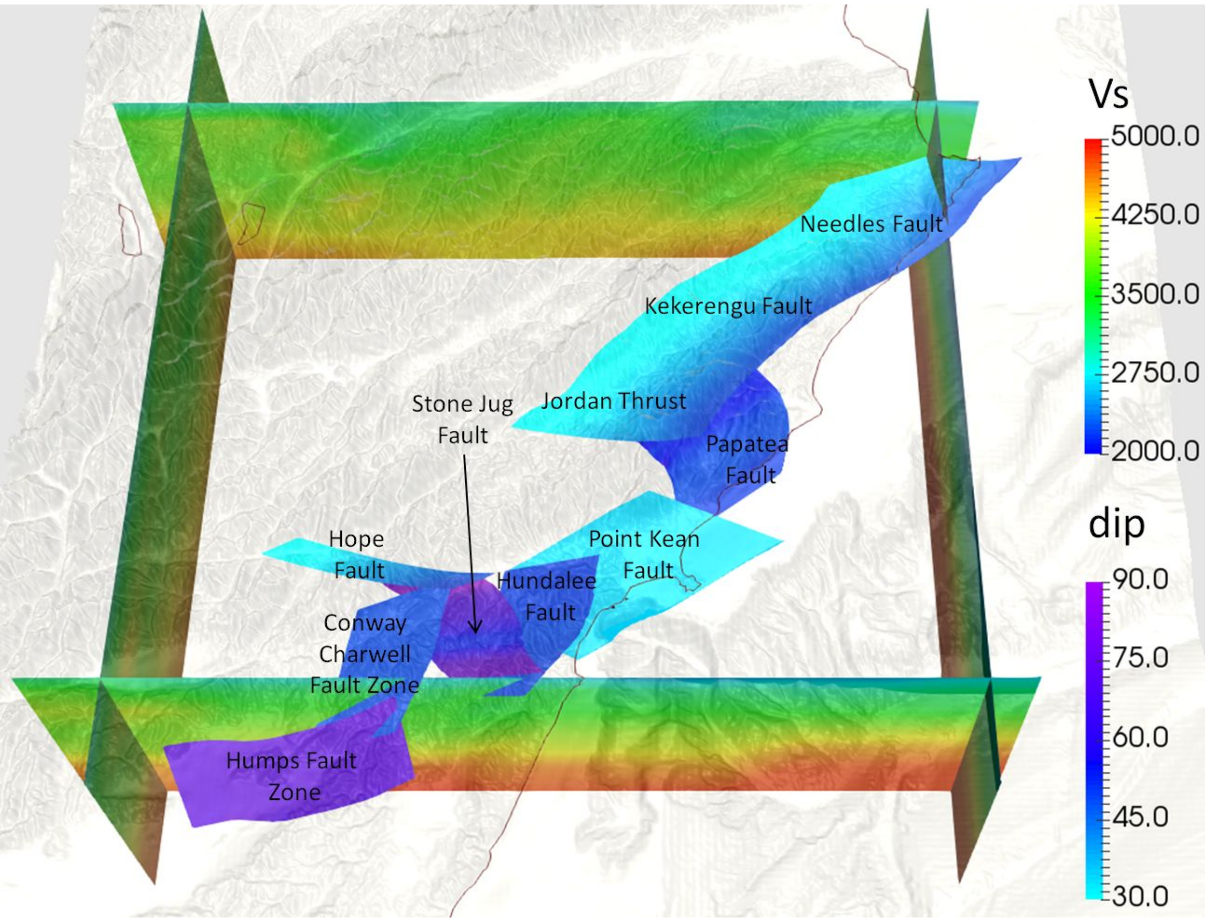

Figure 1: Fault network geometry prescribed for dynamic earthquake rupture modeling. Colors on fault surfaces indicate dipping angle (“dip”), highlighting the flattening with depth of the Hope, Jordan Thrust, Kekerengu and Needles faults. All segments dip westwards, except for the Humps Fault Zone. Also shown are the high-resolution topography and bathymetry (Mitchell et al., 2012) and S-wave speeds (“Vs”) on four cross-sections of the 3D subsurface structure (Eberhart-Phillips et al., 2010) incorporated in the model.

1.2 Friction

We constrain our model parameters based on findings from laboratory to tectonic scale. Specifically, incorporating realistic levels of static and dynamic frictional resistance and stress drop is an important goal in our model design.

We adopt a friction law featuring rapid weakening at high slip velocity (adapted from Dunham et al. (2011) as detailed in methods section A5) which reproduces the dramatic friction decrease observed in laboratory experiments at co-seismic slip rates (Di Toro et al., 2011). Comparing to results of our numerical experiments with linear slip-weakening friction (e.g. Andrews, 1976) on the same fault geometry, we find that strong velocity-weakening facilitates rupture cascading because it yields a smaller critical size to initiate self-sustained rupture by dynamic triggering.

1.3 Initial stresses

The stress and strength of natural faults are difficult to quantify. Although strength parameters are measured in laboratory friction experiments (Di Toro et al., 2011) and estimated from different types of observations (Saffer and Tobin, 2011), little consensus about the actual strength of faults exists (Hardebeck, 2015). We introduce new procedures to constrain the initial fault stress and strength based on seismo-tectonic observations, fault slip inversion models, previous events, deep aseismic creep, fault fluid pressurization and Mohr-Coulomb theory of frictional failure. This systematic approach, detailed in methods section A7, is constrained by observations and simple theoretical analysis. It requires few trial simulations to ensure sustained rupture propagation and reduces the non-uniqueness in dynamic modeling. It is thus superior to the common trial-and-error approach.

A stress state is fully defined by its principal stress magnitudes and orientations. The orientations of all components and the relative magnitude of the intermediate principal stress are here constrained by seismological observations (Townend et al., 2012). In addition, the smallest and largest principal stress components are constrained by applying Mohr-Coulomb theory on a virtual optimally-oriented fault plane (Aochi and Madariaga, 2003). Using static considerations, we first aim for optimal stress parameters within their identified uncertainties, maximizing the ratio of shear over normal stress all over the fault and maximizing the alignment between fault shear tractions and inferred slip (Xu et al., 2018). We then dynamically constrain the amount of initial shear stress and the fluid pressure, aiming for a subshear rupture and slip amounts consistent with results of previous source inversion studies. The resulting model incorporates over-pressurized fault zone fluids (Suppe, 2014; Sutherland et al., 2017; Uphoff et al., 2017) with a fluid pressure equal to 66% of the lithostatic stress.

A favourable stress orientation on all segments, including thrust and strike-slip faults, is promoted by an intermediate principal stress close to the maximum principal stress (Aochi et al., 2006) representing a transpressional regime. This configuration promotes thrust faulting on faults dipping at approximately 60 degrees and striking perpendicularly to the direction of maximum compression, which roughly corresponds with the thrust fault geometries of our model.

Our initial stress model is consistent with the apparent weakness of faults (Copley, 2018, methods section A8). The initial shear to normal stress ratio over most of the seismogenic zone is low (fig. S10). Its median value over the rupture area is 0.09. Earthquake cycle models and geodetic observations of faults loaded by creep on their deeper portions generate a concentration of stresses near the bottom of the seismogenic zone (Kato, 2012, Bruhat and Segall, 2017, Ader et al., 2012). This effect is represented in our model by a band of high initial shear stress along the lower edge of the seismogenic zone. We find that deep stress concentration facilitates dynamic rupture cascading on apparently weak faults, i.e. despite the average shear stress being much lower than the static frictional strength.

Further minor adjustments of the initial stresses are motivated by observations. To prevent thrust faulting of the Kekerengu fault, we introduce a rotation of the maximum compressive stress orientation, within its range of uncertainty, from 100° in the South to 80° in the North. We also introduce a North-South increase of the seismogenic depth to allow deeper slip on the Papatea and Kekerengu faults, which improves the model agreement with observed far-field ground deformations, and prevents shallow supershear rupture, which was not observed. Finally, we locally reduce the initial stresses on the Northernmost part of the Needles fault in a way that mimics the stress shadow caused by the 2013 Cook Strait earthquake sequence (Hamling et al., 2014 and fig. S1). This prevents the occurrence of more than 10 m of fault slip in this area, which is not supported by inversion results (Hamling et al., 2017; Xu et al., 2018).

1.4 Numerical method

We solve the coupled dynamic rupture and wave propagation problem using the freely available software SeisSol (Dumbser and Käser (2006), Pelties et al. (2014), https://github.com/SeisSol/SeisSol) based on the Arbitrary high-order accurate DERivative Discontinuous Galerkin method (ADER-DG). SeisSol employs fully adaptive, unstructured tetrahedral meshes to combine geometrically complex 3D geological structures, nonlinear rheologies and high-order accurate propagation of seismic waves. Our model (fig. 2) includes a geometrically complex fault network, high-resolution topography (Mitchell et al., 2012), 3D subsurface structure (Eberhart-Phillips et al., 2010) and plastic energy dissipation off the fault (Andrews, 2005, Wollherr and Gabriel, 2016). A high resolution model is crucial for accurately resolving rupture branching and (re-)nucleation processes. The degree of realism and accuracy achieved in this study is enabled by recent computational optimizations targeting strong scalability on many-core CPUs (Breuer et al., 2014, Heinecke et al., 2014, Rettenberger et al., 2016) and a ten-fold speedup owing to an efficient local time-stepping algorithm (Uphoff et al., 2017). Simulating 90 seconds on a computational mesh consisting of 29 million elements required typically 2 hours on 3000 Sandy Bridge cores of the supercomputer SuperMuc (Leibniz Supercomputing Centre, Germany). Running hundreds of such simulations is well within the scope of resources available to typical users of supercomputing centres.

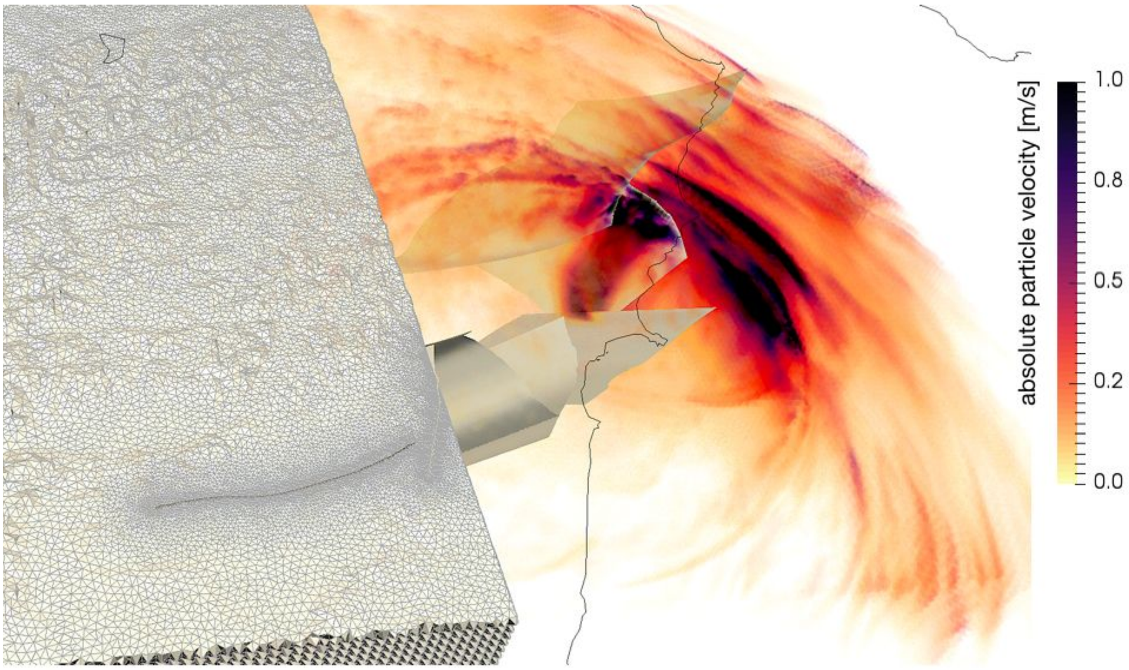

Figure 2: Snapshot of the wavefield (absolute particle velocity in m/s) across the fault network at a rupture time of t=55 s. The model is discretized by an unstructured mesh with refined resolution in the vicinity of the faults, and incorporates the non-linear interactions between frictional on-fault failure, off-fault plasticity and wave propagation throughout 3D subsurface structure and high-resolution topography.

2. Results

In our dynamic model rupture propagates spontaneously across eight fault segments (fig. 1). The combined rupture length exceeds 180 km. The rupture successively cascades from

South to North, directly branching at variable depths from the Humps to the Conwell-Charwell, Hope, Stone Jug, Hundalee and Point Kean faults. It then jumps to the Papatea fault via dynamic triggering at shallow depth, and finally branches to the Jordan Thrust, Kekerengu and Needles faults (fig. 3). This rupture cascade is dynamically viable without slip on an underlying subduction interface. The rupture on the Papatea fault propagates northwards (fig. 2), in agreement with results of high-resolution teleseismic back-projection (Xu et al., 2018).

The modeled slip distributions and orientations are in agreement with the existing results (Xu et al. (2018), Clark et al. (2017)). We observe an alternation of right-lateral strike-slip faulting (Humps, Hope, Jordan Thrust, Kekerengu and Needles faults) and thrusting (Conwell-Charwell, Hundalee and Papatea faults), as well as left-lateral strike-slip rupture of the Stone Jug fault and oblique faulting of the Point Kean fault (fig. 4). Due to the smoothness of our assumed initial stresses, the final slip distribution is less patchy than in source inversion models. However, the moment magnitude of 7.9 is in excellent agreement with observations (fig. 4f).

The complexity of the rupture cascade contributes to its apparently slow rupture speed. The ratio of rupture length to rupture duration (inferred from moment rate functions estimated by various authors; fig. 4f, Bai et al., 2017, Zhang et al., 2017, Vallée et al., 2011) indicates a slow average rupture velocity of about 1.4 km/s (Xu et al., 2018). In our model, rupture along each segment propagates twice as fast, at 2.9 km/s on average. Nevertheless, the observed rupture duration of approximately 90 seconds is reproduced thanks to a zigzagged propagation path accompanied by rupture delays at the transitions between segments (see animations in methods section A1).

Specific episodes of the dynamic rupture model can be associated to prominent phases of moment release and high-frequency radiation observed in the Kaikōura earthquake. Abrupt changes in rupture velocity during the entangled Charwell-Conwell - Hope Fault - Stone Jug fault transition 20 seconds after rupture onset may correspond to a burst of high-frequency energy (Madariaga, 1977) noted by back-projection studies (Zhang et al., 2017; Xu et al., 2018). Around 60 seconds after rupture onset, a distinct moment release burst lasting 20 seconds corresponds to the simultaneous failure of the Papatea and Kekerengu faults and is well aligned with observations (Bai et al., 2017, Zhang et al., 2017, Vallée et al., 2011).

The static ground deformation in our model is in excellent agreement with that inferred from geodetic data (Hamling et al., 2017, Xu et al., 2018, figs. 4 and 5). In particular, the maximum horizontal deformation along the Kekerengu fault and the substantial uplift near the intersection between the Papatea and Kekerengu faults are captured, and the observed ground deformation near the epicenter is reasonably replicated. The deformation in the complex set of faults near the epicenter and the contribution of the Stone Jug fault is overestimated, likely due to neglecting the small-scale complexity of the immature Humps and Charwell-Conwell fault zones (Litchfield et al., 2017).

There is a high level of uniqueness in the outcome of our dynamic models. Slight variations on the initial conditions, for instance a subtle change in the maximum principal stress direction of 10 degrees or a 10% reduction of the magnitude of the intermediate (vertical) principal stress, lead to early spontaneous rupture arrest. Changes in fault geometry (orientation, size and separation distance of fault segments) also affect the dynamics considerably. Moreover, ad hoc abrupt lateral changes in initial fault stress or strength are not required to steer the rupture along its zigzagged path.

Two segments, the Stone Jug and the Point Kean faults, are crucial for the successful propagation of the rupture to the North. The Stone Jug fault hosts little slip but allows the earthquake to branch towards the Hundalee fault. The offshore Point Kean fault links at depth the seemingly disconnected Southern and Northern parts of the fault system (as proposed by Cesca et al., 2017), whose surface traces are separated by a large gap of 15 km. Our model matches the observed (horizontal) surface rupture in the Northern part (Litchfield et al., 2017), the inferred slip amplitude and the northwards rupture propagation on the Point Kean fault, by dominantly oblique faulting. It supports a previous suggestion that rupture of the Point Kean fault was responsible for the observed on-shore coastal uplift extending 20 km north of Kaikōura Peninsula (Clark et al., 2017). On the other hand, a stronger dip-slip component would be required to explain the northeastward GPS displacements around this thrust fault. According to the dynamic rupture model, this could only be achieved by an (unlikely) local prestress rotation of about 30 degrees towards South, or by considering a fault geometry with lower strike.

The dynamic model shows rupture complexity also at a fine scale. Rupture takes the form of slip-pulses (fig. 3) of various origins: fast-velocity weakening friction promotes self-healing slip pulses (Heaton, 1990, Gabriel et al., 2012), the nonlinear interaction between frictional failure and the free surface causes interface waves that bounce back from the surface, fault ends and branching points lead to rupture front segmentation, unloading stresses carried by seismic waves reflected from subsurface impedance contrasts cause healing fronts. The Point Kean, Papatea and Kekerengu segments slip more than once, as in the slip reactivation process inferred from strong-motion waveform inversion (Holden et al., 2017).

Rupture complexity can affect seismological inferences of fault friction properties. Frictional parameters are typically adopted from laboratory experiments. However, it is uncertain how valid it is to extrapolate results from the laboratory scale to the field scale. For the Kaikōura earthquake, a large slip-weakening distance D_c has been estimated from a strong-motion record (Kaneko et al., 2017). Despite the much smaller on-fault D_c values (0.2 to 0.5 m) in our model, the apparent D_c value inferred from the resulting off-fault ground motions is large (5.6 m, fig. S4), which can be attributed to intertwined waveforms from multiple slip fronts.

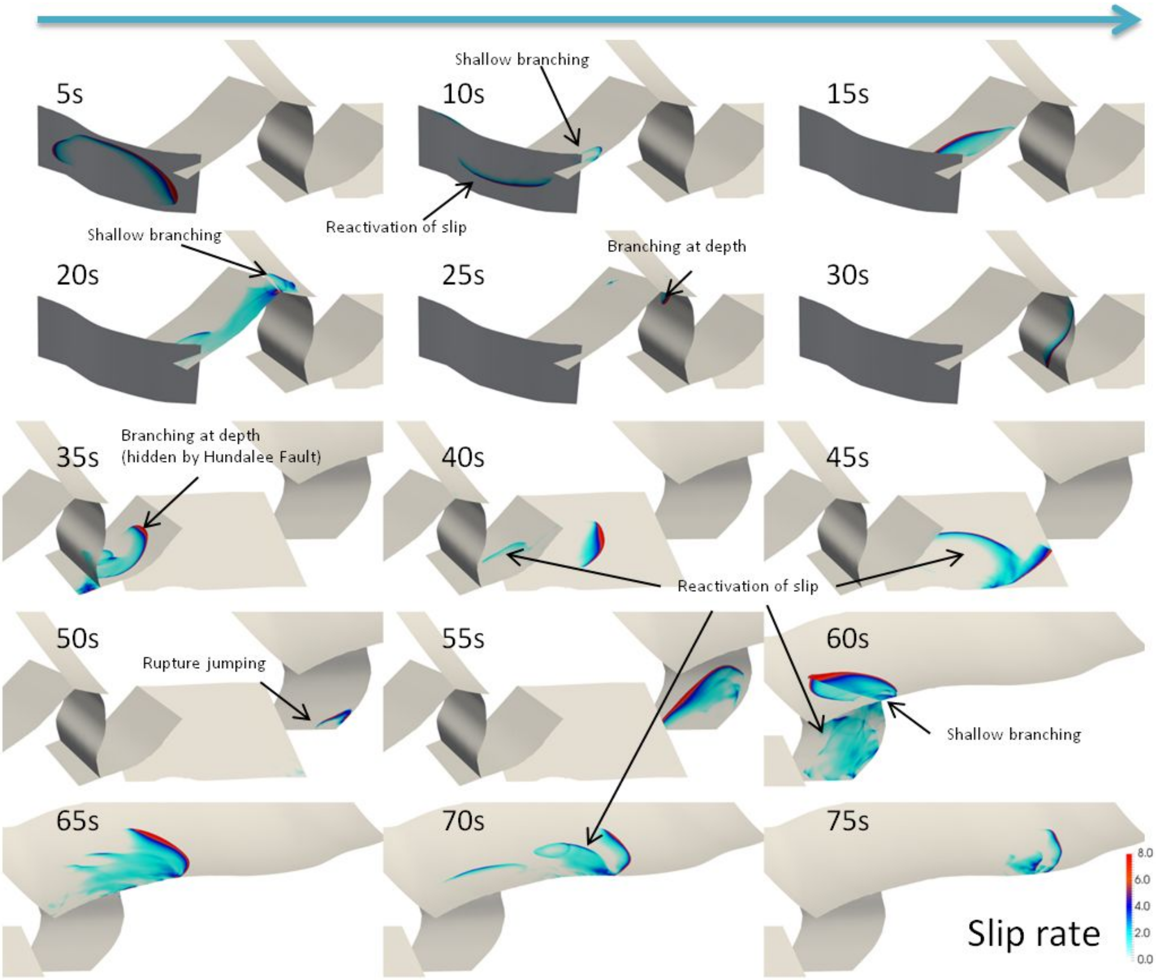

Figure 3: Overview of the simulated rupture propagation. Snapshots of the absolute slip rate every 5 s. The figure focuses on three different portions of the fault system, following the rupture front as it propagates from South to North. Labels indicate remarkable features of the rupture discussed in the text.

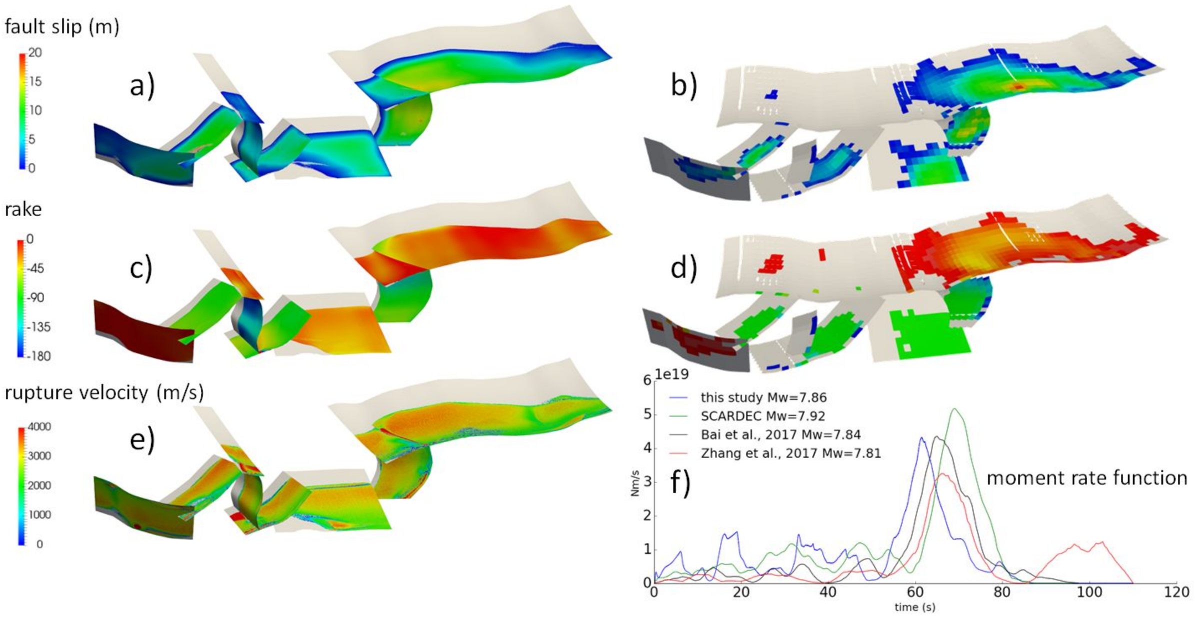

Figure 4: Source properties of the dynamic rupture model and comparison to observational inferences. Final slip magnitude (a) modeled here and (b) inferred by Xu et al. (2018). Final rake angle (c) modeled and (d) inferred by Xu et al. (2018). (e) Modeled rupture velocity. (f) Modeled moment rate function compared with those inferred by Bai et al. (2017) from teleseismic and tsunami data, by Zhang et al. (2017) from seismic waveform inversion and by the SCARDEC method (Vallée et al., 2011).

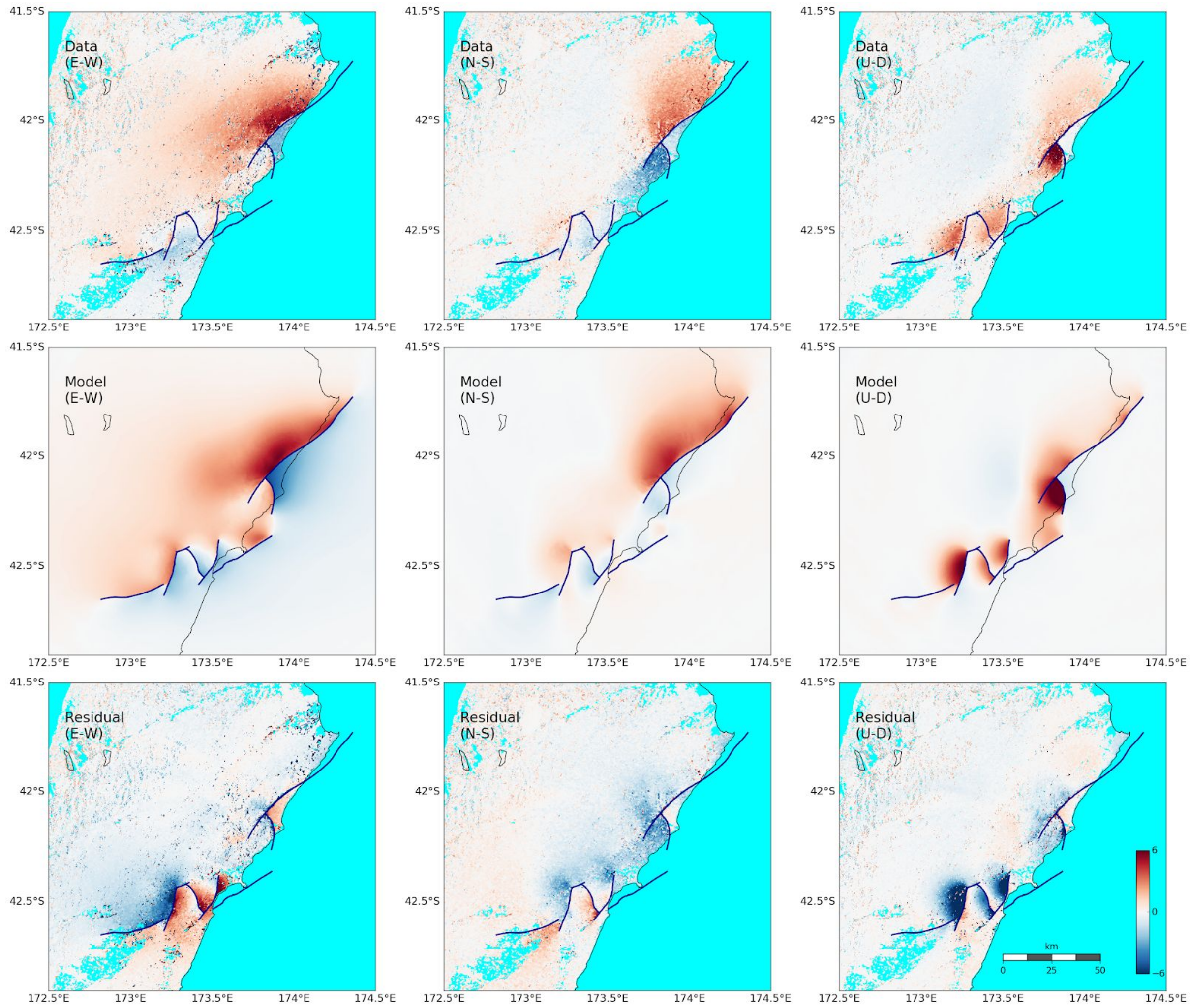

Figure 5: Comparison of observed and modeled coseismic surface displacements. 3D ground displacement (first row) inferred by space geodetic data (Xu et al. 2018), (second row) generated by the dynamic rupture model and (third row) their difference, all in meters. Columns from left to right are EW, NS and UD components.

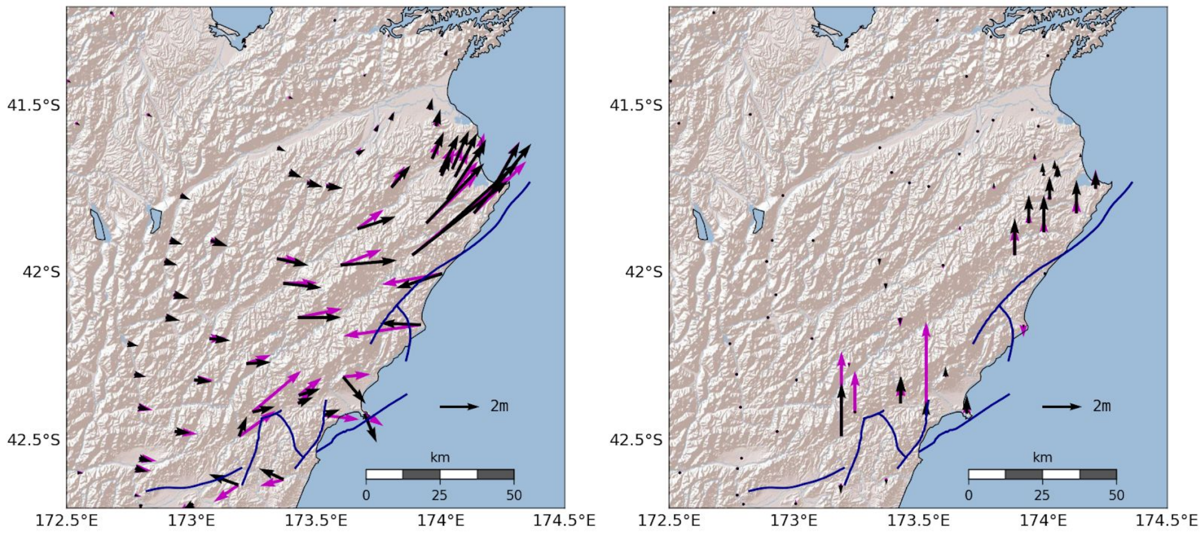

Figure 6: Comparison of observed (black, Hamling et al. 2017) and modeled (magenta) horizontal (left) and vertical (right) ground displacement at GPS stations.

3. Discussion

Our results provide insight on the state of stress in which complex fault systems operate. The model demonstrates that the apparent weakness of faults, i.e. their low average ratio of initial shear stress to normal stress (Copley, 2017), does not hinder dynamic rupture cascading across multiple fault segments if dynamic triggering is facilitated by deep interseismic stress concentration. Such stress state combined with strong frictional weakening and fluid overpressure results in a remarkably low apparent friction (see methods section A8). The conjunction of these three effects and the fundamental impact of fault weakness on the existence of subduction and tectonics (e.g. Osei Tutu et al., 2018) show the importance of mechanical feedbacks across multiple time scales, from the short-term processes of dynamic rupture and earthquake cycles to the long-term geodynamic processes that shape and reshape the Earth.

Frictional failure initiates at the best-oriented fault segment, in contrast with the 'keystone fault' model (Fletcher et al., 2016) in which large multi-fault earthquakes nucleate on a misoriented fault. The dynamic rupture cascade does not require laterally heterogeneous initial stresses, as those arising on fault networks in which optimally oriented faults release stress not only during large earthquakes but also via smaller events or aseismic creep.

Physics-based dynamic modeling contributes crucial arguments to the debate of whether the rupture of multiple crustal faults during the Kaikōura earthquake was promoted by slip on the underlying subduction interface. Rupture of the subduction interface is not favored by the regional stresses, because the resolved shear stress on a shallowly dipping subduction interface is low. Dynamic triggering of the subduction interface is further impeded by its large depth below the crustal fault network. However, slip may be promoted if stresses rotate at depth or if the megathrust is weak (i.e. if it has a very low friction coefficient, Hardebeck et al., 2015). We show that incorporating the shallowly dipping (35 degrees) Point Kean fault segment successfully links the Southern and Northern parts of the fault system without involvement of the Hikurangi subduction interface, a model that may be further tested with tele-seismic and tsunami data.

Features of the Kaikōura earthquake that remain unexplained by our dynamic models suggest opportunities to understand better the role of fault heterogeneities. The lack of significant slip observed on the Hope fault is surprising given its orientation similar to the Kekerengu fault, its fast geologic slip-rate and short recurrence interval (180-310 years, Stirling et al. (2017) and references herein), and its linkage to most mapped faults involved in the rupture. If we include the Hope fault in our dynamic model, it breaks entirely and with significant slip. Under the assumption of smooth regional stresses, explaining the non-rupture of the Hope fault requires strength heterogeneities, due for instance to heterogeneous fault zone fluid pressure. An alternative interpretation is stress heterogeneity, in particular stress released by past earthquakes on the Hope fault.

Dynamic rupture modeling is now approaching a state of maturity and computational efficiency that should soon allow it to be integrated synergistically with data inversion efforts within the first days following the occurrence of an earthquake, making physics-based interpretations an important part of the rapid earthquake response toolset.

Acknowledgments

The work presented in this paper was supported by the German Research Foundation (DFG) (projects no. KA 2281/4-1, GA 2465/2-1, GA 2465/3-1), by BaCaTec (project no. A4), by KONWIHR - the Bavarian Competence Network for Technical and Scientific High Performance Computing (project NewWave), by the Volkswagen Foundation (grant no. 88479), by KAUST-CRG (grant no. ORS-2016-CRG5-3027), by the European Union’s Horizon 2020 research and innovation program (grant no. 671698), NSF CAREER award EAR-1151926, the Hong Kong Polytechnic University startup grant (1-ZE6R) and the Hong Kong Research Grants Council Early Career Scheme Fund (Project No. F-PP4B). Computing resources were provided by the Leibniz Supercomputing Centre (LRZ, projects no. h019z, pr63qo, and pr45fi on SuperMUC). We thank J. Townend for sharing his stress inversion data, and J. Zhang and M. Vallée for sharing moment rate functions.

Author contributions

This project was initiated by J.-P. A. Modelling was conducted by T. U. under the supervision of A.-A. G. with input from J.-P. A. and W. X. The initial manuscript was developed by T. U. and T. U., A.-A. G. and J.-P. A. contributed equally to major edits for the final manuscript.

Competing interests

The authors declare no competing financial interests.

References

1. Hamling, I. J. et al. (2017). Complex multifault rupture during the 2016 Mw 7.8 Kaikōura earthquake, New Zealand. *Science*, **356** (6334), 7194.
2. Duputel, Z., and Rivera, L. (2017). Long-period analysis of the 2016 Kaikoura earthquake. *Physics of the Earth and Planetary Interiors*, **265**, 62-66.
3. Bradley, B. A., Razafindrakoto, H. N., and Polak, V. (2017). Ground-Motion Observations from the 14 November 2016 M w 7.8 Kaikoura, New Zealand, Earthquake and Insights from Broadband Simulations. *Seismological Research Letters*, **88** (3), 740-756.
4. Holden, C. et al. (2017). The 2016 Kaikōura Earthquake Revealed by Kinematic Source Inversion and Seismic Wavefield Simulations: Slow Rupture Propagation on a Geometrically Complex Crustal Fault Network. *Geophysical Research Letters*, **44** (22), 11320-11328.
5. Wang, T. et al. (2018). The 2016 Kaikōura earthquake: Simultaneous rupture of the subduction interface and overlying faults. *Earth and Planetary Science Letters*, **482**, 44-51.

6. Hollingsworth, J., Ye, L., and Avouac, J. P. (2017). Dynamically triggered slip on a splay fault in the Mw 7.8, 2016 Kaikoura (New Zealand) earthquake. *Geophysical Research Letters*, **44** (8), 3517-3525.

7. Xu, W. et al. (2018). Transpressional Rupture Cascade of the 2016 M_w 7.8 Kaikoura Earthquake, New Zealand. *Journal of Geophysical Research: Solid Earth*, **123**.

8. Zhang, H., Koper, K. D., Pankow, K., and Ge, Z. (2017). Imaging the 2016 MW 7.8 Kaikoura, New Zealand Earthquake with Teleseismic P Waves: A Cascading Rupture Across Multiple Faults. *Geophysical Research Letters*, **44**, 4790-4798.

9. Bai, Y., Lay, T., Cheung, K. F., and Ye, L. (2017). Two regions of seafloor deformation generated the tsunami for the 13 November 2016, Kaikoura, New Zealand earthquake. *Geophysical Research Letters*, **44** (13), 6597-6606.

10. Clark, K. J. et al. (2017). Highly variable coastal deformation in the 2016 Mw7. 8 Kaikōura earthquake reflects rupture complexity along a transpressional plate boundary. *Earth and Planetary Science Letters*, **474**, 334-344.

11. Cesca, S. et al. (2017). Complex rupture process of the Mw 7.8, 2016, Kaikoura earthquake, New Zealand, and its aftershock sequence. *Earth and Planetary Science Letters*, **478**, 110-120.

12. Williams, C. A. et al. (2013). Revised interface geometry for the Hikurangi subduction zone, New Zealand. *Seismological Research Letters*, **84**(6), 1066-1073.

13. Bai, K., and Ampuero, J. P. (2017). Effect of Seismogenic Depth and Background Stress on Physical Limits of Earthquake Rupture Across Fault Step Overs. *Journal of Geophysical Research: Solid Earth*, **122** (12), 10280-10298.

14. Gabriel, A.-A., Ampuero, J. P., Dalguer, L. A., and Mai, P. M. (2012). The transition of dynamic rupture styles in elastic media under velocity-weakening friction. *Journal of Geophysical Research: Solid Earth*, **117** (B9), B09311.

15. Shi, Z., and Day, S. M. (2013). Rupture dynamics and ground motion from 3-D rough-fault simulations. *Journal of Geophysical Research: Solid Earth*, **118** (3), 1122-1141.

16. Aochi, H., and Ulrich, T. (2015). A probable earthquake scenario near Istanbul determined from dynamic simulations. *Bulletin of the Seismological Society of America*, ***105*** (3), 1468-1475.

17. Olsen, K. B., Madariaga, R., and Archuleta, R. J. (1997). Three-dimensional dynamic simulation of the 1992 Landers earthquake. *Science*, **278** (5339), 834-838.

18. Ma, Custódio, Archuleta, and Liu (2008), Dynamic modeling of the 2004 Mw 6.0 Parkfield, California, earthquake, *J. Geophys. Res.*, **113**, B02301.

19. Townend, J., Sherburn, S., Arnold, R., Boese, C., and Woods, L. (2012). Three-dimensional variations in present-day tectonic stress along the

Australia–Pacific plate boundary in New Zealand. *Earth and Planetary Science Letters*, **353**, 47-59.

20. Brune, J. N., Henyey, T. L. and Roy, R. F. (1969). Heat flow, stress, and rate of slip along the San Andreas fault, California, *Journal of Geophysical Research,* **74** (15), 3821–3827.

21. Copley, A. (2018). The strength of earthquake-generating faults. *Journal of the Geological Society*, **175** (1), 1-12.

22. Byerlee, J. D. (1978) Friction of Rocks. *Pure and Applied Geophysics*. **116** (4-5), 615–626.

23. Litchfield N. J., et al. (2017). 14th November 2016 M7.8 Kaikoura Earthquake. Summary surface fault rupture traces and displacement measurements. GNS Science.

24. Mitchell, J. S. et al. (2012). Undersea New Zealand, 1:5,000,000.

25. Eberhart-Phillips, D., Reyners, M., Bannister, S., Chadwick, M., and Ellis, S. (2010). Establishing a versatile 3-D seismic velocity model for New Zealand. *Seismological Research Letters*, **81** (6), 992-1000.

26. Dunham, E. M., Belanger, D., Cong, L., and Kozdon, J. E. (2011). Earthquake ruptures with strongly rate-weakening friction and off-fault plasticity, Part 1: Planar faults. *Bulletin of the Seismological Society of America*, **101**(5), 2296-2307.

27. Di Toro, G. et al. (2011). Fault lubrication during earthquakes. *Nature*, **471** (7339), 494.

28. Andrews, D. J. (1976). Rupture propagation with finite stress in antiplane strain. *Journal of Geophysical Research*, ***81*** (20), 3575-3582.

29. Saffer, D. M., and Tobin, H. J. (2011). Hydrogeology and mechanics of subduction zone forearcs: Fluid flow and pore pressure. *Annual Review of Earth and Planetary Sciences*, **39**, 157-186.

30. Hardebeck, J. L. (2015). Stress orientations in subduction zones and the strength of subduction megathrust faults. *Science*, **349** (6253), 1213-1216.

31. Aochi, H., and Madariaga, R. (2003). The 1999 Izmit, Turkey, earthquake: Nonplanar fault structure, dynamic rupture process, and strong ground motion. *Bulletin of the Seismological Society of America*, ***93*** (3), 1249-1266.

32. Suppe, J. (2014). Fluid overpressures and strength of the sedimentary upper crust. *Journal of Structural Geology*, **69**, 481-492.

33. Sutherland, R. et al. (2017). Extreme hydrothermal conditions at an active plate-bounding fault. *Nature*, **546** (7656), 137.

34. Uphoff, C., Rettenberger, S., Bader, M., Madden, E. H., Ulrich, T., Wollherr, S., and Gabriel, A.-A. (2017. Extreme scale multi-physics simulations of the tsunamigenic

2004 Sumatra megathrust earthquake. In *Proceedings of the International Conference for High Performance Computing, Networking, Storage and Analysis,* SC'17, 21, 1-16.

35. Aochi, H., Cushing, M., Scotti, O., and Berge-Thierry, C. (2006). Estimating rupture scenario likelihood based on dynamic rupture simulations: The example of the segmented Middle Durance fault, southeastern France. *Geophysical Journal International*, ***165*** (2), 436-446.

36. Kato, N. (2012). Fracture energies at the rupture nucleation points of large interplate earthquakes. *Earth and Planetary Science Letters*, **353**, 190-197.

37. Bruhat, L., and Segall, P. (2017). Deformation rates in northern Cascadia consistent with slow updip propagation of deep interseismic creep. *Geophysical Journal International*, **211**(1), 427-449.

38. Ader, T., et al. (2012). Convergence rate across the Nepal Himalaya and interseismic coupling on the Main Himalayan Thrust: Implications for seismic hazard. *Journal of Geophysical Research: Solid Earth*, **117** (B4), B04403.

39. Hamling, I. J. et al. (2014). Crustal deformation and stress transfer during a propagating earthquake sequence: The 2013 Cook Strait sequence, central New Zealand. *Journal of Geophysical Research: Solid Earth*, **119** (7), 6080-6092.

40. Dumbser, M. and Käser, M. (2006). An Arbitrary High Order Discontinuous Galerkin Method for Elastic Waves on Unstructured Meshes II: The Three-Dimensional Isotropic Case. *Geophysical Journal International*, **167**(1), 319-336.

41. Pelties, C., Gabriel, A.-A., and Ampuero, J. P. (2014). Verification of an ADER-DG method for complex dynamic rupture problems. *Geoscientific Model Development*, **7** (3), 847-866.

42. Andrews, D. J. (2005). Rupture dynamics with energy loss outside the slip zone. *Journal of Geophysical Research: Solid Earth*, **110** (B1), B01307.

43. Wollherr, S., and Gabriel, A.-A. (2016). Off-fault plasticity in dynamic rupture simulations: 3D numerical analysis and effects on rupture transfer in complex fault geometries. *2016 SCEC Annual Meeting Abstracts,* 62, SCEC Contribution 6733.

44. Breuer, A. et al. (2014). Sustained petascale performance of seismic simulations with SeisSol on SuperMUC. In *International Supercomputing Conference,* ISC 2014, 8488, 1-18.

45. Heinecke, A. et al. (2014). Petascale high-order dynamic rupture earthquake simulations on heterogeneous supercomputers. In *Proceedings of the International Conference for High Performance Computing, Networking, Storage and Analysis*, SC’14, 3-14.

46. Rettenberger, S., Meister O., Bader M., and Gabriel A.-A. (2016), ASAGI - A Parallel Server for Adapative Geoinformation, in 2016 Exascale Applications and Software Conference (EASC2016) Proceedings, doi:10.1145/2938615.2938618.

47. Vallée, M., Charléty, J., Ferreira, A. M., Delouis, B., and Vergoz, J. (2011). SCARDEC: a new technique for the rapid determination of seismic moment magnitude, focal mechanism and source time functions for large earthquakes using body-wave deconvolution. *Geophysical Journal International*, **184** (1), 338-358.

48. Madariaga, R. (1977). High-frequency radiation from crack (stress drop) models of earthquake faulting. *Geophysical Journal International*, **51** (3), 625-651.

49. Heaton, T. H. (1990). Evidence for and implications of self-healing pulses of slip in earthquake rupture. *Physics of the Earth and Planetary Interiors*, **64** (1), 1-20.

50. Kaneko, Y., Fukuyama, E., and Hamling, I. J. (2017). Slip-weakening distance and energy budget inferred from near-fault ground deformation during the 2016 Mw7. 8 Kaikōura earthquake. *Geophysical Research Letters,* **44** (10), 4765-4773.

51. Osei Tutu, A., Sobolev, S. V., Steinberger, B., Popov, A. A., and Rogozhina, I. (2018). Evaluating the influence of plate boundary friction and mantle viscosity on plate velocities. *Geochemistry, Geophysics, Geosystems*, **19.**

52. Fletcher, J. M., Oskin, M. E., and Teran, O. J. (2016). The role of a keystone fault in triggering the complex El Mayor-Cucapah earthquake rupture. *Nature Geoscience*, **9** (4), 303-307.

53. Stirling, M. W. et al. (2017). The Mw 7.8 2016 Kaikōura earthquake: Surface fault rupture and seismic hazard context. *Bull. New Zeal. Soc. Earthq. Eng.*, **50** (2), 73-84.

Methods

A1. Animations

A. Slip rate animation

https://syncandshare.lrz.de/getlink/fia7W6N8G4NQUpWunHMYuhs/NZ_SR_090318-cp.mov

B. Slip rate and wavefield animation

https://syncandshare.lrz.de/getlink/fiUPLyk7qZeTJ69Q9Pcii1D8/NZ_wavefield_SR_090318-cpx4.mov

A2. Data availability

The authors declare that all data supporting the findings of this study are available within the paper and its methods section. In particular, all data required to run a simulation of the Kaikōura earthquake can be downloaded from https://syncandshare.lrz.de/getlink/fi6ZynFEZ1KbUgKPNdUVSQaa/. We used the SeisSol (branch easi, version tag 201803_Kaikoura) available on Github. The procedure to download, compile and run the code is described on the wiki (https://github.com/SeisSol/SeisSol/wiki).

A3. Geometry of the fault system

Our starting point is the fault network geometry "model III" proposed by Xu et al. (2018). Fig. S1 illustrates our main modifications of their model. We first smooth the model using a Discrete Smooth Interpolation function (Mallet, 1992) to remove artificial fault kinks caused by the coarseness of the original discretisation. We then compute explicitly the intersection between the faults and the surface topography to accurately account for the possibility of surface rupture in our model. The original geometry of the Stone Jug fault (displayed as a wireframe in fig. S1) does not connect the Hope and Hundalee faults and thus prevents rupture transfer. We base this model's Stone Jug fault geometry on the observed fault surface rupture (Litchfield et al., 2017) which we extend at depth following realistic dipping angles. We extend the Point Kean fault to the South to allow rupture branching from the Hundalee Fault. To the North, the Point Kean fault is about 2 km away from the Papatea fault. As justified in the main text (section 1.1), most of the Hope and Upper Kowai faults is removed. We also remove the part of the Hundalee fault that did not experience much slip, according to Xu et al. (2018).

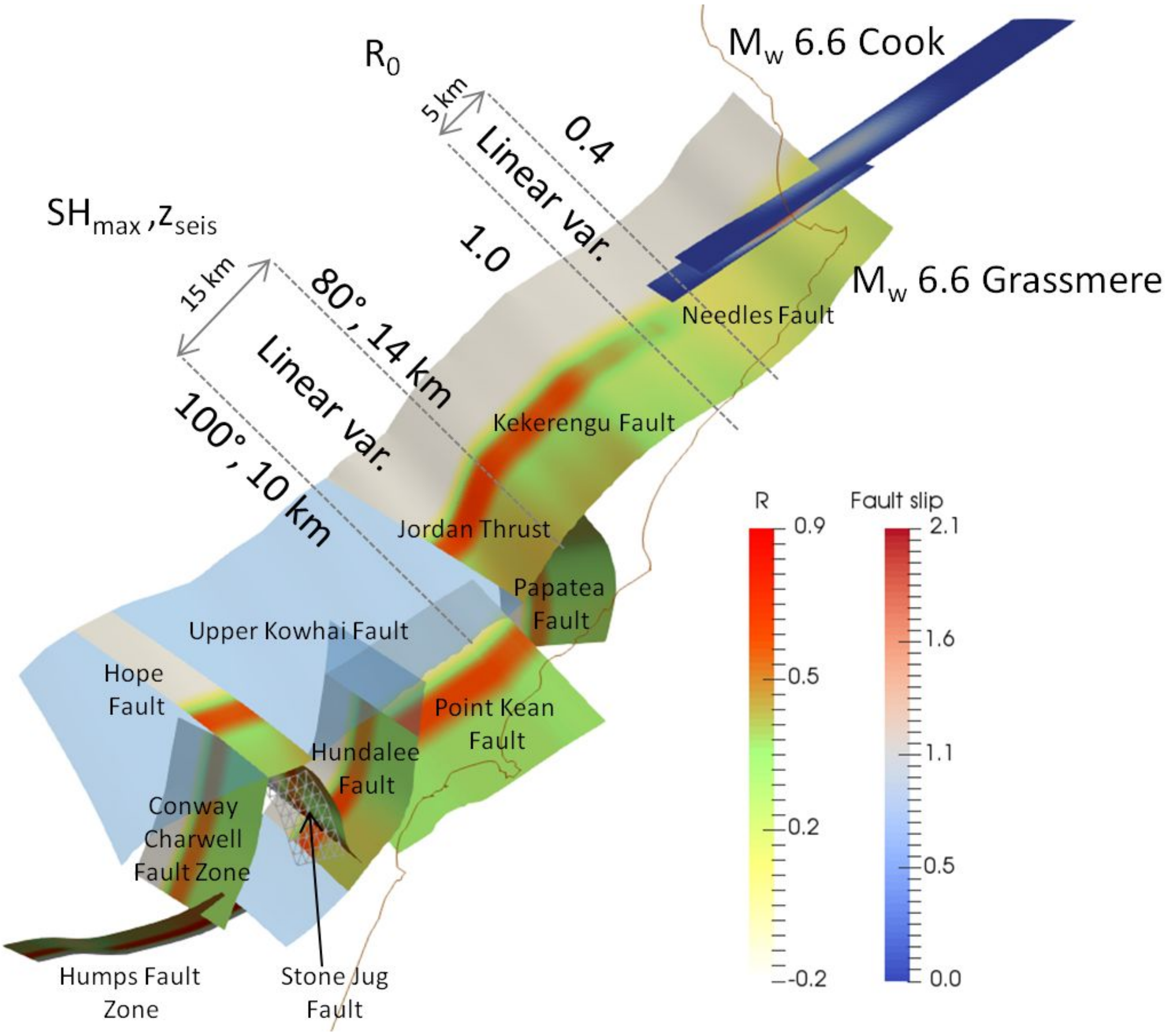

Figure S1: Adaptations made on the fault geometry of Xu et al. (2018) to develop a realistic dynamic rupture model. Fault areas shown in transparent blue are trimmed. Xu et al. (2018)'s Stone Jug fault geometry is shown as a wireframe. The distribution of initial fault stress ratio R (eq. 1) along the fault network is also shown. The spatial distributions of parameters defining the stress (SH_{max}, R and z_{seis} defined hereafter) are indicated. The magnitude decrease of the initial stress loading in the Needle fault region (here modeled by the decrease of R_0 by 60% combined with the suppression of the deep stress concentrations in that region) is the consequence of the Cook strait sequence, illustrated here by the final slip of each event from Hamling et al. (2014).

A4. Mesh

The domain is discretized into an unstructured computational mesh of 29 million high-order (spatio-temporal order 4) four-node linear tetrahedral elements (fig. 2). The mesh resolution is refined to element edge lengths of 300 m close to faults. Topography and bathymetry are discretized by at most 1000 m and refined in regions of strong variations. The mesh allows resolving the seismic wavefield at frequencies up to 3 Hz in the vicinity of the faults.

A5. Fault friction

We use a rate- and state-dependent friction law with fast velocity-weakening at high speed proposed in the community benchmark problem TPV104 of the Southern California Earthquake Center (Harris et al., 2018) and similar to the friction law introduced by Dunham et al. (2011). Here we provide the governing equations using the notations defined in Table 1. The magnitude of the shear traction τ is assumed to always equal the fault strength, defined as the product of the friction coefficient f and the effective normal stress σ_n:

$$\tau = f(V, \psi)\sigma_n \qquad \text{(eq. 1)}$$

The traction $\overline{\tau}$ and slip rate $\overline{V}$ vectors are parallel and satisfy:

$$\tau\overline{V} = V\overline{\tau} \qquad \text{(eq. 2)}$$

The friction coefficient f depends on the slip rate V and a state variable ψ:

$$f(V, \psi) = a\ arcsinh\,(\tfrac{V}{2V_0} exp(\tfrac{\psi}{a})) \qquad \text{(eq. 3)}$$

The state variable ψ evolves according to the following differential equation:

$$\frac{d\psi}{dt} = -\frac{V}{L}(\psi - \psi_{ss}(V)) \qquad \text{(eq. 4)}$$

where ψ_{ss} is the value of the state variable at steady-state given by:

$$\psi_{ss}(V) \ = \ a \ ln \ (\frac{2V_0}{V} sinh(\frac{f_{ss}(V)}{a})) \qquad \text{(eq. 5)}$$

where the steady-state friction coefficient is

$$f_{ss}(V) \ = f_w \ + \ \frac{f_{LV}(V) - f_w}{(1 + (V/V_w)^8)^{1/8}} \qquad \text{(eq. 6)}$$

and the low-velocity steady-state friction coefficient f_{LV} is given by:

$$f_{LV}(V) = f_0 - (b - a) ln(V/V_0) \qquad \text{(eq. 7)}$$

At slip rates higher than the characteristic slip rate V_w, f_{ss} asymptotically approaches the fully weakened friction coefficient f_w, with a decay roughly proportional to $1/V$. This feature of friction is observed in laboratory experiments and is present in thermal weakening theories. At low slip velocities, this friction law is consistent with classical rate-and-state friction.

The initial distribution of the state variable ψ_{ini} is obtained, from eqs. (1) and (3), assuming that the faults are initially at steady state, sliding at a slip rate of magnitude V_{ini} = 10^{-16} m/s:

$$\psi_{ini} = a\ ln\ (\frac{2V_0}{V_{ini}} sinh(\frac{\tau_{ini}}{a\sigma_{ini}})) \qquad \text{(eq. 8)}$$

where τ_{ini} and σ_{ini} are the (spatially varying) initial shear and normal tractions on the fault.

The values of the frictional properties adopted in this study are given in Table 1. Some parameters are depth dependent, as indicated in fig. S2. To suppress shallow supershear transition, V_w is assumed to be larger at shallow depth (e.g. Shi and Day, 2013) on all faults (except for the Conway-Charwell segment, to avoid suppressing its emerging shallow rupture quickly after branching from the Humps fault).

Table 1: Fault frictional properties used in this study.

Direct-effect parameter	a	0.01
Evolution-effect parameter	b	0.014
Reference slip rate	V_0	10^{-6} m/s
Steady-state low-velocity friction coefficient at slip rate V_0	f_0	0.6
Characteristic slip distance of state evolution	L	0.2 m
Weakening slip rate	V_w	0.1 m/s
Fully weakened friction coefficient	f_w	0.1
Initial slip rate	V_{ini}	10^{-16} m/s

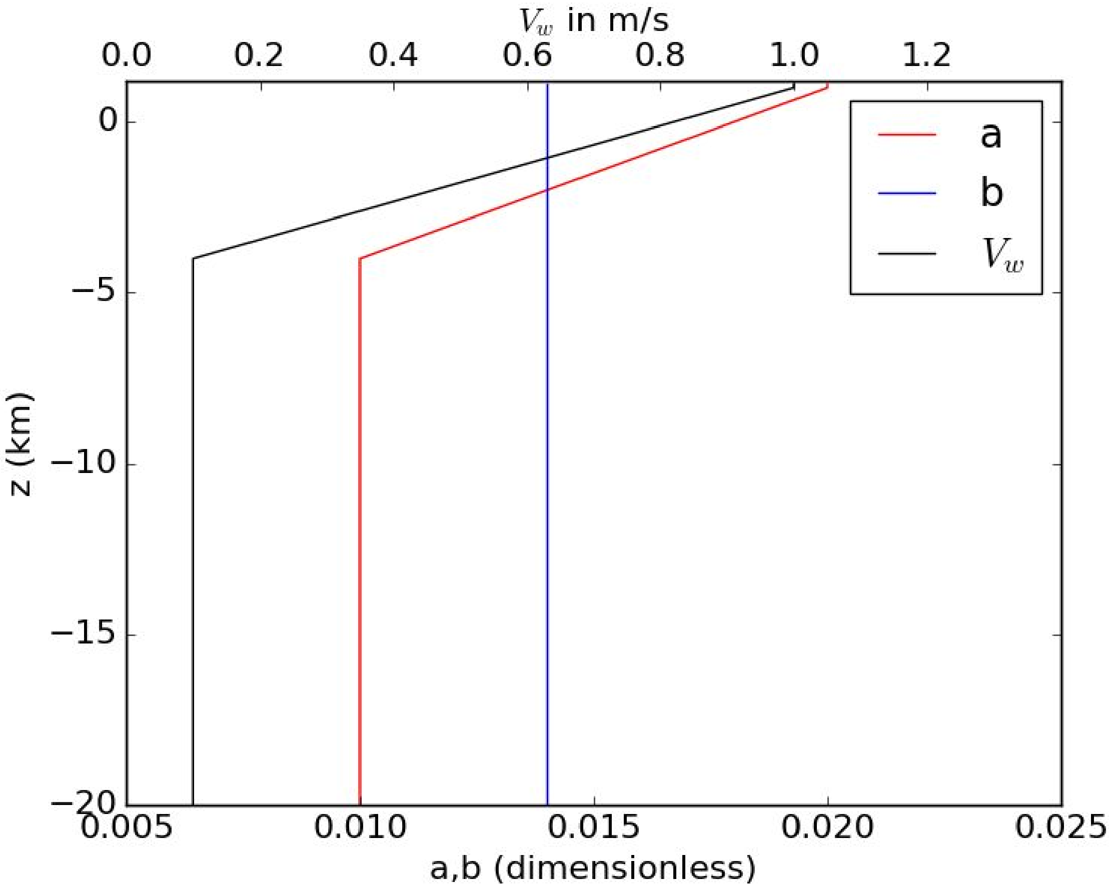

Figure S2: Depth dependence of friction parameters.

We infer the equivalent slip-weakening distance Dc_{eq} of our simulations from the resulting curves of shear stress as a function of slip at various points along the rupture. We define

$$Dc_{eq} = 2\, G_c/(\tau_{peak} - \tau_{final}) \qquad \text{where} \quad G_c = \int_{D_{peak}}^{\infty} (\tau(D) - \tau_{final})dD$$

Fig. S3 shows the typical stress change at 5 fault locations. The values of Dc_{eq} fall in the range from 0.2 to 0.5 m. In addition, following Kaneko et al. (2017), we apply the method of Mikumo et al. (2003) to our modeled seismograms at station KEKS (fig. S4) to estimate an apparent slip-weakening distance Dc" defined as twice the fault-parallel displacement at the time the peak fault-parallel velocity is reached. The fault-parallel velocity waveform has two peaks of similar amplitude, separated by a few seconds, which may result from multiple slip fronts on the Kekerengu fault (see animation B in methods section A1). We estimate D_c'' = 1.2 m from the first peak. The second peak gives D_c'' = 5.6 m, similar to the value of 4.9 m estimated by Kaneko et al. (2017). These D_c'' estimates are larger than the on-fault Dc_{eq} for at least three reasons. First, the station is at a distance from the fault (~2.7 km) much larger than the maximum distance for resolution of Mikumo et al. (2003)'s method ($R_c = 0.8V_sT_c =$ 232 m, where $V_s =$2.9 km/s is the shear wave velocity and $T_c =$0.1 s is the breakdown time. Note that T_c in our simulations is much smaller than the apparent value of 5.5 s reported by Kaneko et al. (2017)). Second, off-fault plasticity (included in our model) can contribute to increase the apparent D_c''. Third, our dynamic model features multiple slip fronts contributing to the cumulative fault-parallel displacement, thus increasing D_c''.

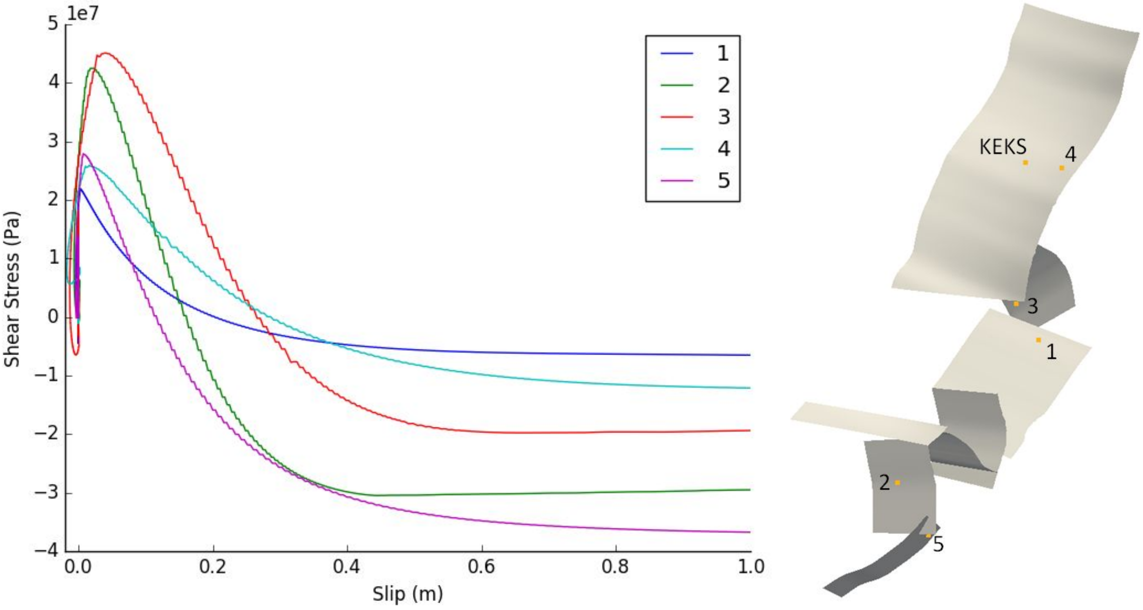

Figure S3: Slip-weakening response and equivalent critical slip-weakening distance. (a) Changes of shear traction in the direction of initial shear traction as a function of slip at 5 fault locations shown in (b). The stress drops over slip distances in the range from 0.2 to 0.5 m.

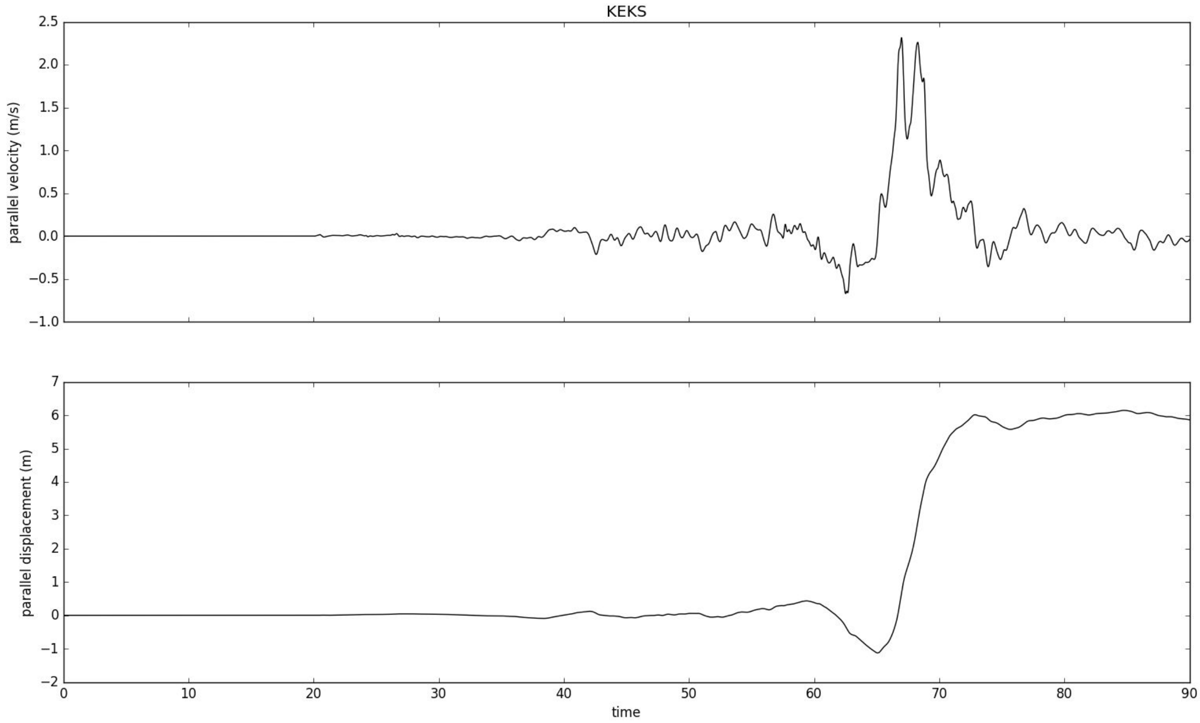

Figure S4: Fault-parallel velocity and displacement synthetic waveforms at station KEKS (fig. S3b) and estimation of apparent slip-weakening distance D_c'' following the method of Mikumo et al. (2003) defined as twice the fault-parallel displacement observed when the peak fault-parallel velocity is reached. We estimate D_c'' = 5.6 m averaging over multiple parallel velocity peaks caused by segmented on-fault dynamic rupture fronts.

A6. Off-fault plasticity

We model off-fault dissipation assuming a Drucker-Prager elasto-viscoplastic rheology (Wollherr and Gabriel, 2016). The failure criterion is parameterized by two material properties, internal friction coefficient and cohesion. We set the internal friction coefficient equal to the reference fault friction coefficient (0.6). Following Roten et al. (2017), we consider an empirically-motivated depth-dependent distribution of cohesion (fig. S5) to account for the tightening of the rock structure with depth. Lower cohesion in the upper 6 km allows suppressing the unrealistic occurence of shallow supershear transitions without preventing rupture cascading by dynamic triggering. A viscoplastic relaxation mechanism is adopted to ensure convergence of the simulation results upon mesh refinement. Its relaxation time T_v also controls the effectiveness of plasticity. We set T_v=0.05 s, independently of the mesh resolution. We consider depth-dependent off-fault initial stresses consistent with the initial stresses prescribed on the fault.

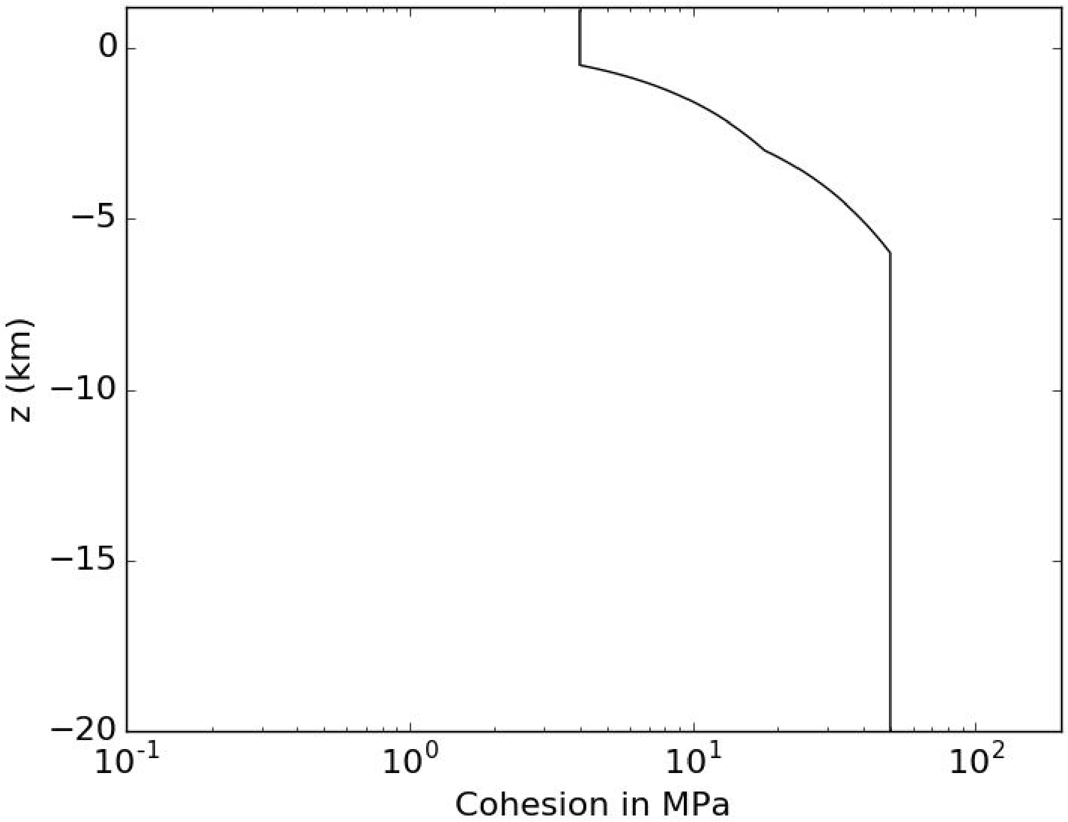

Figure S5: Depth dependence of cohesion in the off-fault plastic yielding criterion.

A7. Initial stresses

We set the initial stresses in the rupture area based on regional stress parameters inferred from earthquake focal mechanisms by Townend et al (2012). Among the earthquake clusters they considered, the ones within our region of interest are, from North to South, clusters 27, 65, 16, 11 and 18 (fig. S6-a). We ignore cluster 53, located between 50 and 100 km depth, because it is much deeper than the Kaikōura earthquake source. The stress parameters at the considered clusters are shown in fig. S6-b, along with their uncertainties. The average azimuth of the maximum horizontal compressive stress SH_{max} (Lund and Townend, 2007) is 96° (the average over the whole South Island is 115°). The stress shape ratio $= (s_2 - s_3)/(s_1 - s_3)$, where s_k are the amplitudes of the principal stresses, is most likely around 0.5 to 0.6, but higher values cannot be ruled out. The orientation of the intermediate principal stress relative to the horizontal plane falls in the range 80° to 110°.

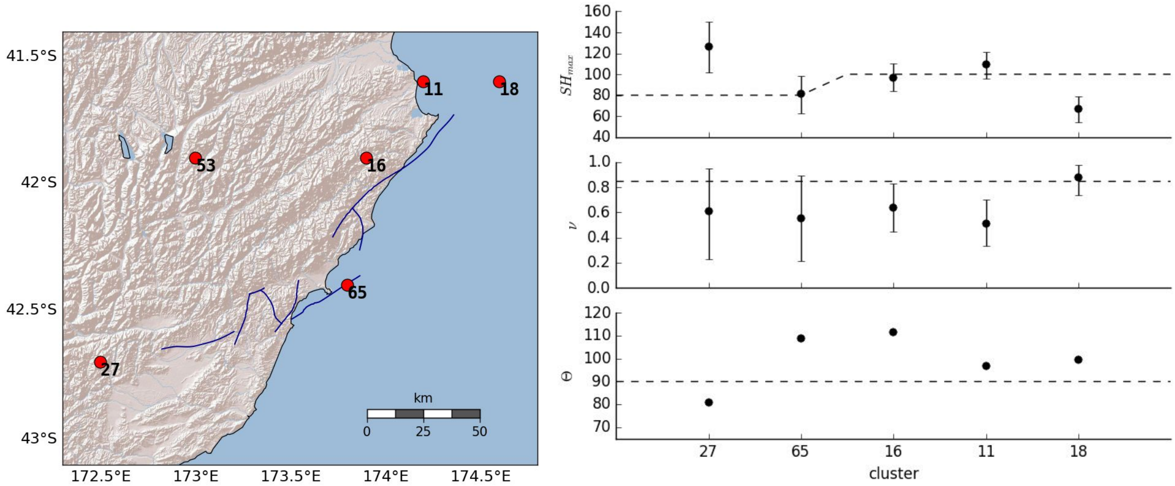

Figure S6: (a) Centroid locations of the earthquake clusters from Townend et al (2012) that are close to the Kaikōura earthquake source. We discard cluster 53 because it is too deep. (b) Stress parameters of the 5 remaining clusters. Uncertainties of SH_{max} and are indicated by their 10% - 90% percentile ranges (vertical bars). The dashed lines show the stress parameter values we chose.

Following Townend et al (2012), we parameterize the initial stress tensor using SH_{max} , and . Following Lund and Townend (2007), SH_{max} is defined as the azimuth of maximum horizontal compressive stress, and does not necessarily coincide with the commonly used horizontal projection of the largest subhorizontal stress (both definitions coincide if the state of stress is Andersonian, i.e. if one principal component is vertical). An additional parameter, the relative prestress ratio R between fault stress drop and breakdown strength drop, allows constraining the magnitude of the deviatoric stresses:

$$R = \frac{\tau - \mu_d \sigma_n}{(\mu_s - \mu_d)\, \sigma_n} \qquad \text{(eq. 9)}$$

To compute R we assume $\mu_d = f_w = 0.1$, as we observe that the fully weakened friction f_w is typically reached in our simulations. The maximum friction coefficient reached during rupture is not a prescribed constant friction parameter. Its value varies along the fault and often exceeds f_0 but rarely falls below this value. For simplicity, we use $\mu_s = f_0 = 0.6$ as a conservative value: in our simulation results, the real R can be smaller than the one we prescribe but is rarely larger.

Following the notations of Aochi and Madariaga (2003), we define

$$P = (s_1 + s_3)/2 \text{ and } ds = (s_1 - s_3)/2\,. \qquad \text{(eq. 10)}$$

$(P, 0)$ is the center of the Mohr-Coulomb circle and ds is its radius. The s_i are related to P, ds and by:

$$s_1 = P + ds,$$
$$s_2 = P - ds + 2\ \ ds \qquad \text{(eq. 11)}$$
$$s_3 = P - ds$$

The effective confining stress $\sigma_c' = (s_1 + s_2 + s_3)/3$ is related to P by:

$$\sigma_c' = P + (2 - 1)\ ds/3 \qquad \text{(eq. 12)}$$

We assume fluid pressure throughout the crust is proportional to the lithostatic stress ($P_f = \gamma\ \sigma_c(z)$, where γ is the fluid-pressure ratio) and derive $\sigma_c'(z) = (1 - \gamma)\ \sigma(z)$. We set $\sigma_c(z) = \rho g z$, where the rock density is $\rho = 2670$ kg/m^3. The value $\gamma = \rho_{water}/\rho = 0.37$ corresponds to a hydrostatic state; higher values $\gamma > 0.37$ correspond to overpressurized states.

The shear and normal stress τ and σ_n on a fault plane oriented at an angle Φ relative to the maximum principal stress are:

$$\tau = ds\ sin(2\Phi)$$
$$\sigma_n = P - ds\ cos(2\Phi) \qquad \text{(eq. 13)}$$

An optimally oriented fault plane is one that, under homogeneous initial stress and stressing rate, would reach failure before any other fault with different orientation. At failure, its shear to normal stress ratio is maximized (compared to other fault orientations) and equal to μ_s. Its angle is:

$$\Phi = /4 - 0.5\, atan(\mu_s) \qquad \text{(eq. 14)}$$

We will prescribe $R_{opt}(z) = R_0\, g(z)$ on the (virtual) optimally oriented fault plane, where $g(z)$, described hereafter, is a stress modulation function accounting for stress concentrations expected right above the seismogenic depth of faults loaded by deep fault creep. Using eqs. 9, 12 and 13, we solve for ds and obtain:

$$ds = \frac{\sigma_c'}{sin(2\Phi)/(\mu_d + (\mu_s - \mu_d)R_{opt}) + (2v-1)/3 + cos(2\Phi)} \qquad \text{(eq. 15)}$$

For given values of   and R_0, we can compute the depth-dependent s_i using eqs. 11, 12 and 15. The orientations of the three principal stress components (assumed depth-independent) are determined by the angles SH_{max} and   and by the constraint that the faulting mechanism on the optimally oriented plane is strike-slip. This defines a depth-dependent stress tensor (b_{ij}). The final stress tensor (s_{ij}) is obtained by applying a second stress modulation function $\Omega(z)$, which smoothly cancels the deviatoric stresses below the seismogenic depth z_{seis}:

$$s_{ij} = \Omega(z)\, b_{ij}(z) + (1 - \Omega(z))\, \sigma_c'(z)_{\ ij} \qquad \text{(eq. 16)}$$

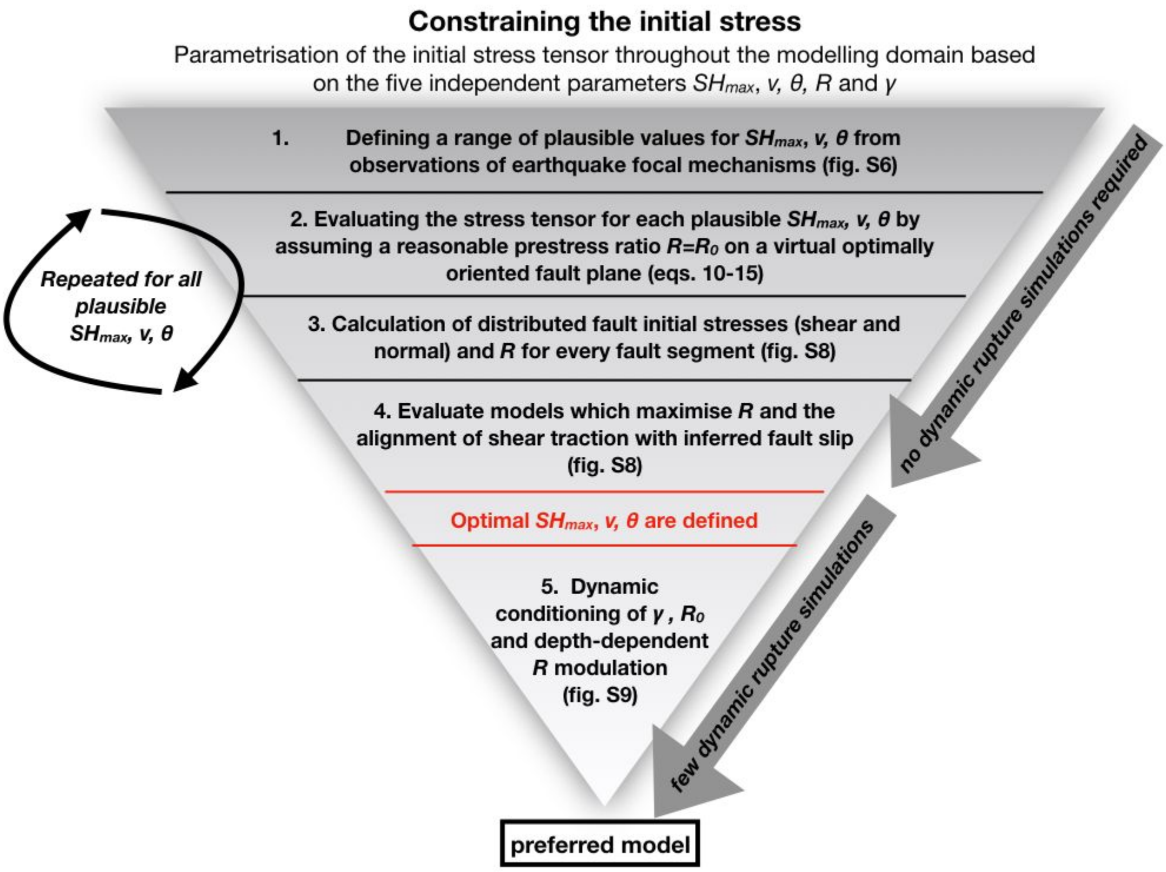

Figure S7: Workflow for constraining the initial stress from observations and simple theoretical analysis requiring only few trial dynamic rupture simulations. Five independent parameters fully describe the initial stress tensor: SH_{max} denotes the azimuth of maximum horizontal compressive stress, is the stress shape ratio, is the orientation of the intermediate principal stress relative to horizontal, R is the relative prestress ratio and γ is the ratio between fluid-pressure and lithostatic confining stress, all defined in the text.

The initial stress model depends on several parameters that have uncertainties: SH_{max} , , , R_0 and $g(z)$. To determine the preferred values adopted in our final simulations, instead of running costly dynamic rupture simulations for each parameter set, we developed the following workflow, illustrated in fig. S7.

In a first step, we constrain SH_{max} , and to ensure compatibility of the stress with inferred fault geometry and slip rake. As a first assumption, we use a fluid-pressure ratio $\gamma = 0.75$ (Uphoff et al., 2017). We set uniform stress modulation functions, $g(z) = 1$ and $\Omega(z) = 1$, and assume $R_{opt}(z) = R_0 = 0.7$ on the optimal plane. We expect this R_0 value to be high enough to allow a sustained rupture on faults of highly varying orientations and low enough to result in a reasonable stress drop (an order-of-magnitude estimate of stress drop is $R_0\,(1-\gamma)\sigma_c\,(\mu_s - \mu_d)$). We test different stress configurations, by varying SH_{max} in the range 50°-120°, in the range 0.5-1 and in the range 70°-110°. For each value of the (SH_{max} , ,) triplet we do the following: compute the principal stress components using equations 10-15; obtain the principal stress orientations from SH_{max} , and the additional constraint that the faulting mechanism of the optimal plane is strike-slip; compute and visualize the distribution of R and of the shear-stress traction orientation resolved on the fault system (fig. S8). We then select the stress configuration (SH_{max} , ,) that maximizes R all along the fault system, especially around rupture transition zones to enable triggering, and that optimizes the alignment between initial fault shear tractions and the slip directions inferred by Xu et al. (2018). We rerun the procedure with a lower and a larger R_0 (0.5 and 0.9, respectively) to confirm that the conclusion obtained with $R_0 = 0.7$ still holds. In the next step of our stress setup we will determine the preferred value of R_0 based on dynamic considerations.

Fig. S8 presents a few of the many cases we tested. Eight examples are shown, which correspond to all permutations of the following values: SH_{max} = 100° and 115°, = 80° and 90°, =0.5 and 0.85. The value =0.5 results in a favorable stress orientation only for the Humps Fault Zone. Higher values of v are required to obtain a favorable stress orientation on the other faults. Our preferred value is =0.85. The value SH_{max} =100° achieves the best overall alignment between initial shear tractions and target slip on all faults. We find that the angle has a limited influence within the range tested, and thus opt for the simplest assumption of an Andersonian stress regime: = 90°.

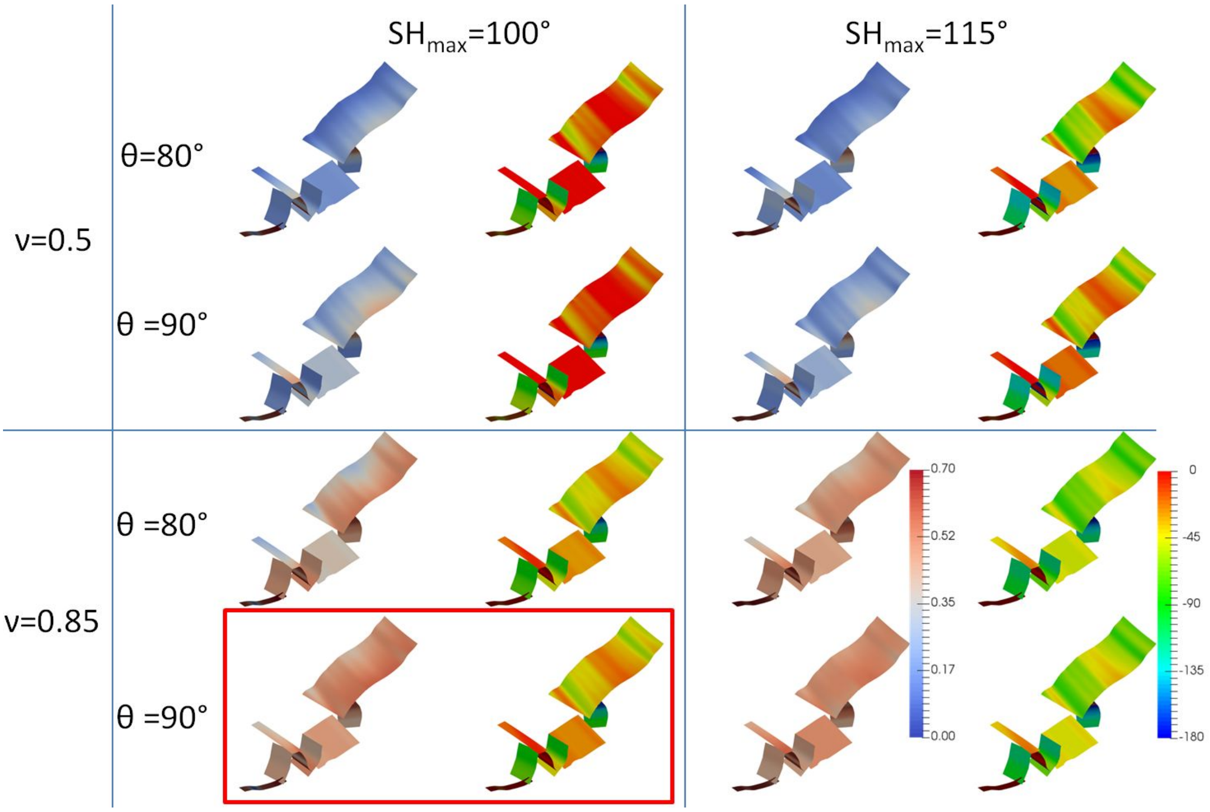

Figure S8: A representative sample of initial stress models tested. We show 8 examples that correspond to all permutations involving the two values indicated in the labels for each stress parameter, SH_{max} , and . For each example, two plots show the spatial distribution on the fault surfaces of (left) the pre-stress ratio and (right) the rake angle of the shear traction. Here we assume a uniform $R_{opt}(z) = 0.7$ on the optimal plane.

In a second step, we constrain γ, R_0 and the shape of the initial stress modulation functions, $g(z)$ and $\Omega(z)$, to allow the rupture to cascade along the whole fault system with a realistic amount of fault slip. This is done by trial-and-error based on dynamic rupture simulations. To save computational resources, we do the trial simulations on a coarser mesh (except near the fault) and only run the initial 25 s to test if the most challenging Hope-Stone Jug fault transition can be overcome. We set the depth z_{seis}, at which $\Omega(z)$ starts to decrease, equal to the average maximum depth of the slip patches inferred by Xu et al. (2018). We set the width of the stress concentration area (the depth range above z_{seis} in which $g(z) = 1$) and the value of R_0 (0.87) just large enough to overcome the difficult Hope-Stone Jug fault transition. Both $g(0)$ and affect the average stress drop, $d \sim R_0 g(0)(\mu_s - \mu_d)(1 - \gamma)\sigma_c$, and thus the average slip. High values of $g(0)(1 -)$ lead to supershear rupture and unrealistically large slip, low values result in rupture terminating too early. The trade-off between $g(0)$ and γ is nevertheless mitigated by physical constraints on $g(0)$: a too small value of $g(0)$ would lead to a stress drop too peaked in the deeper portion of the rupture (too marked stress concentration), which would be inconsistent with slip models from source inversion. Nevertheless, resolving the detailed shape of such stress concentration might be challenging because finite source inversion and interseismic geodetic studies suffer from poorer resolution at depth and entail smoothing due to regularization. We choose $g(0) = 0.6$ and $= 0.66$, which ensure a subshear rupture and slip amounts consistent with results of previous source inversion studies. Fig. S9 depicts the resulting shape of the initial stress modulation functions $g(z)$ and $\Omega(z)$. We note that variations in fault geometry, for instance a more favourable geometry of the challenging Conwell Charwell - Hope - Stone Jug faults transition, might allow a more homogeneous stress profile (with $g(0)$ closer to 1) combined with a lower R_0.

We also consider a small lateral variation in the regional stress, summarized in fig. S1 and described in the main text.

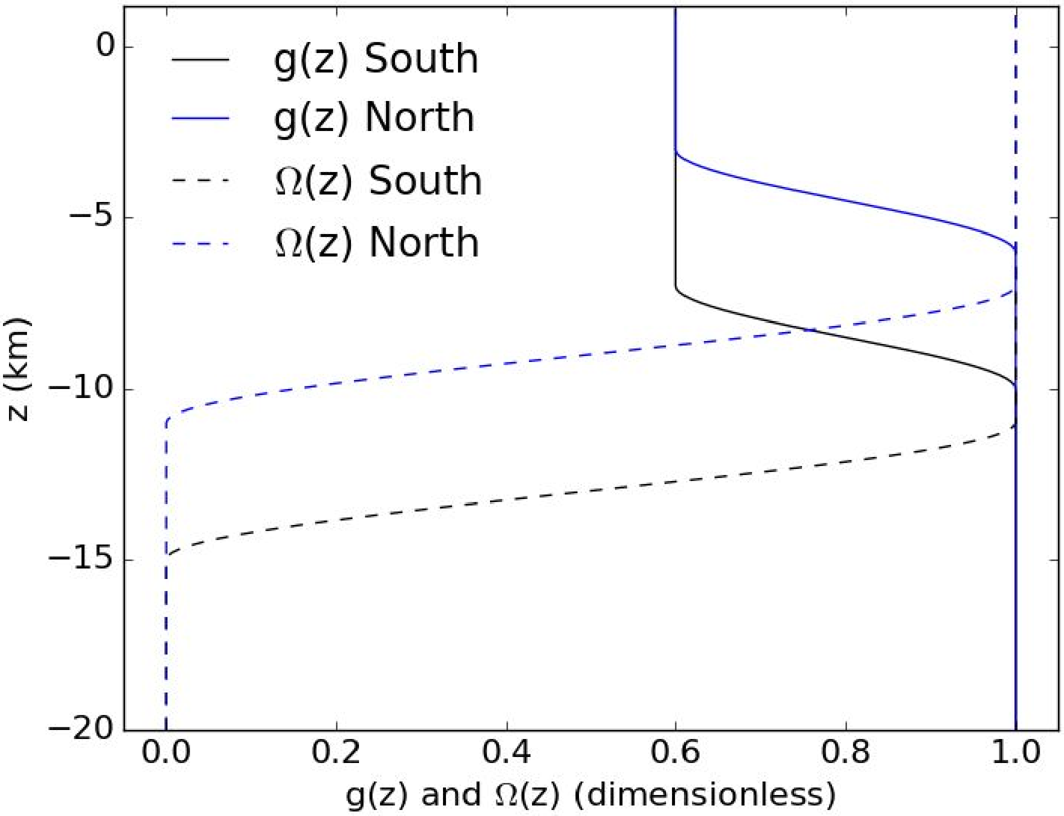

Figure S9: Depth-dependent stress modulation functions $g(z)$ and $\Omega(z)$. The former tapers off at some distance above the seismogenic depth z_{seis} and the latter tapers off below z_{seis}, which is taken shallower in the Northern part of the rupture than in its Southern part.

A8. Apparent fault weakness

In our preferred model, overpressurized fault fluids and deep stress concentrations lead to a low value of the initial shear to normal stress ratio over most of the seismogenic zone (fig. S10). These two ingredients and the additional effect of a low dynamic friction result in an low apparent friction coefficient μ^* which can be approximated as:

$$\mu^* \sim (\mu_d + (\mu_s - \mu_d)g(0)R_0)(1-\gamma), \qquad \text{(eq. 17)}$$

This estimate allows us to quantify the relative contribution of each effect: fluid overpressure $(1-\gamma)$, deep stress concentration ($g(0)R_0$) and dynamic weakening (μ_d). In our preferred model $\mu_d = 0.1$, $(1-\gamma) = 0.33$ and $(\mu_s - \mu_d)g(0)R_0) = 0.26$. Without the stress concentration, a high R_0 would be needed for a viable rupture cascade ($g(0)R_0 \approx 1$) and extreme fluid overpressure and dynamic weakening would be needed to achieve $\mu^* < 0.1$ and a reasonable stress drop. We thus conclude that the three effects are important in allowing complex fault systems to operate at low apparent friction, and that our findings warrant studies of the mechanical feedbacks between long-term geodynamic processes and the short-term processes of dynamic rupture and earthquake cycles.

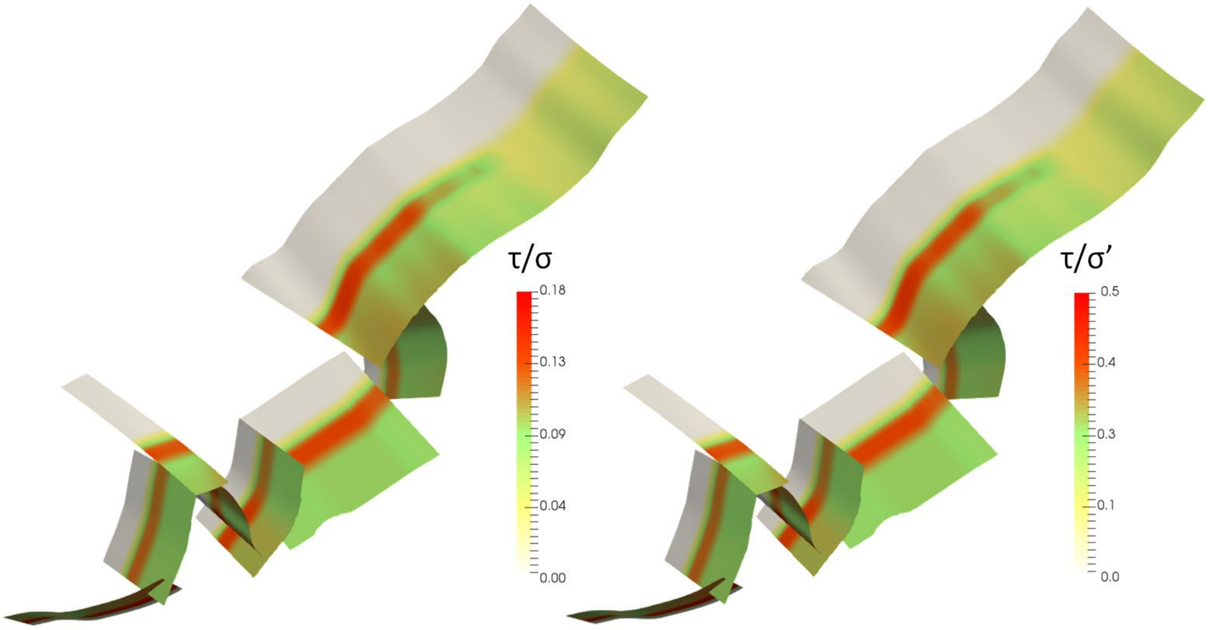

Figure S10: Ratio of initial shear stress over normal stress (left) and over effective normal stress (right).

A9. Rupture nucleation

Rupture is nucleated by overstressing an area centered at the hypocenter, smoothly in space and time. This is achieved by increasing the initial relative prestress ratio R_0 as:

$$R_{0\,nuc} = R_0 + F(r)\,G(t) \qquad \text{(eq. 18)}$$

F(r) is a Gaussian shaped function:

$F(r) \;=\; 5\,exp(\frac{r^2}{r^2-r_c^2})$ if $r < r_c$,

= 0 elsewhere (eq. 19)

where $r_c = 2$ km is the nucleation radius. The coefficient 5 is determined by trial on error numerical experiments to allow nucleation of sustained sub-shear rupture. $G(t)$ is a smoothed step function:

$$G(t) = \begin{cases} exp\left(\frac{(t-T)^2}{t(t-2T)}\right) & \text{if } 0<t<T \\ 1 & \text{if } t \geq T \end{cases} \qquad \text{(eq. 20)}$$

where $T = 0.5$ s is the nucleation time.

Additional References

1. Mallet, J. L. (1992). Discrete smooth interpolation in geometric modelling. *Computer-aided design*, ***24*** (4), 178-191.

2. Mikumo, T., Olsen, K. B., Fukuyama, E., and Yagi, Y. (2003). Stress-breakdown time and slip-weakening distance inferred from slip-velocity functions on earthquake faults. *Bulletin of the Seismological Society of America*, **93** (1), 264-282.

3. Harris, R. A. et al. (2018). A suite of exercises for verifying dynamic earthquake rupture codes. *Seismological Research Letters*, (accepted for publication).

4. Roten, D., Olsen, K. B., Day, S. M., & Cui, Y. (2017). Quantification of fault-zone plasticity effects with spontaneous rupture simulations. *Pure and Applied Geophysics*, **174** (9), 3369-3391.

5. Lund, B., and Townend, J. (2007). Calculating horizontal stress orientations with full or partial knowledge of the tectonic stress tensor. *Geophysical Journal International*, **170** (3), 1328-1335.